



# Niobium oxide confined by ceria nanotubes as a novel SCR catalyst with excellent resistance to potassium, phosphorus, and lead



Penglu Wang<sup>a,b</sup>, Si Chen<sup>a,b</sup>, Shan Gao<sup>a,c</sup>, Jingyi Zhang<sup>d</sup>, Haiqiang Wang<sup>a,b,\*</sup>, Zhongbiao Wu<sup>a,b</sup>

<sup>a</sup> Key Laboratory of Environment Remediation and Ecological Health, Ministry of Education, College of Environmental & Resources Science, Zhejiang University, Hangzhou 310058, PR China

<sup>b</sup> Zhejiang Provincial Engineering Research Center of Industrial Boiler & Furnace Flue Gas Pollution Control, Hangzhou 310027, PR China

<sup>c</sup> Zhejiang Tianlan Environmental Protection Technology Co., Ltd., Hangzhou 311202, PR China

<sup>d</sup> Shanghai Superconductor Technology Co., Ltd., Shanghai, 200080, PR China

## ARTICLE INFO

### Keywords:

Ceria nanotubes  
Niobia  
SCR  
Deactivation  
Resistance

## ABSTRACT

In this study, a novel niobia-doped ceria nanotubes material (Nb-CeNTs) is synthesized and used as deNO<sub>x</sub> catalyst. For comparison, a nanoparticle sample is also obtained by doping CeO<sub>2</sub> nanoparticles with niobia (Nb-CeO<sub>2</sub>(N)). The Nb-CeNTs catalyst shows superior NO<sub>x</sub> conversion and resistance to alkali metals, phosphorus, and lead than Nb-CeO<sub>2</sub>(N) for selective catalytic reduction (SCR) by NH<sub>3</sub>. After subjected to a range of characterization techniques, it is found that the enhanced resistance is mainly attributed to the special nanotubular structure of ceria nanotubes, smooth Nb<sup>5+</sup>/Nb<sup>4+</sup> and Ce<sup>4+</sup>/Ce<sup>3+</sup> redox cycles, superior redox capacity, and abundant surface Brønsted acidic sites. Moreover, the well-maintained nanotubular structure also accounts for the excellent resistance performance of the Nb-CeNTs catalyst. We foresee that the remarkable chemical properties and self-protection effect of the Nb-CeNTs catalyst may provide a novel approach for the design and synthesis of SCR catalysts to improve the resistance to different kinds of poisons, such as alkali/alkaline earth metals, phosphorus compounds, and heavy metals.

## 1. Introduction

NO<sub>x</sub> is one of the main air pollutants that can cause serious environmental problems such as acid rain, photochemical smog and haze weather. To control the emission of nitric oxides from power plants, industrial boilers, and other combustion processes of fossil fuels, selective catalytic reduction (SCR) of NO<sub>x</sub> by NH<sub>3</sub> in O<sub>2</sub> is one of the most efficient technologies [1–4]. Although commercial V<sub>2</sub>O<sub>5</sub>–WO<sub>3</sub>/TiO<sub>2</sub> and V<sub>2</sub>O<sub>5</sub>–MoO<sub>3</sub>/TiO<sub>2</sub> catalysts have achieved excellent reduction performance, catalyst deactivation emerges as the largest obstacle for application of SCR technology in recent years. The flue gas is identified to contain various amount of catalyst poisons, e.g. alkali/alkaline metals such as K [5], Na [6], and Ca [7]; phosphorus compounds [8]; heavy metals such as arsenic [9], lead [10–12] and mercury [13,14]. Furthermore, the wide use of biomass in power plants as a fossil fuel alternative makes the deactivation of deNO<sub>x</sub> catalysts by alkali/alkaline metals and phosphorus compounds more and more serious [15–19]. Moreover, alkali metals decrease the amount of acidic surface sites by covering the active metal surface and damaging the catalyst structure [7,20]. For phosphorus compounds, the loss of active sites, formation of

vanadyl phosphate, and pore blocking by phosphoric acid or phosphorus oxide are reported to cause the deactivation of V-based catalysts [8,21]. Furthermore, it is reported that with regard to waste incinerators, the concentration of Pb in dust is up to 30 mg/g and 6–40 mg/m<sup>3</sup> in the flue gas before electrostatic precipitators (ESP). The resulting deactivation of the catalyst by PbO is mainly ascribed to its competitive chemisorption on the acidic sites and decreasing of surface acidity and reducibility [10–12]. Consequently, to solve the deactivation of SCR catalyst, plenty of novel materials, such as CeO<sub>2</sub>–MoO<sub>3</sub> [8], CeO<sub>2</sub>–WO<sub>3</sub> [22], CeO<sub>2</sub>/SO<sub>4</sub><sup>2-</sup>–ZrO<sub>2</sub> [23], MnO<sub>x</sub>–CeO<sub>x</sub>/CNTs [24], and CeO<sub>2</sub>/TNTs [25] have been studied and reported. However, most of these materials only focus on the deactivation of one poison for the deNO<sub>x</sub> catalyst, e.g. CeO<sub>2</sub>/SO<sub>4</sub><sup>2-</sup>–ZrO<sub>2</sub> and CeO<sub>2</sub>/TNTs mainly investigate the poisoning mechanism by alkali/alkaline metals [23,25], while CeO<sub>2</sub>–MoO<sub>3</sub> relies on a promotion mechanism to alleviate phosphate poisoning [8]. Vanadia-based catalysts and CeO<sub>2</sub>/TiO<sub>2</sub> are reported to study the deactivation effect of lead [10–12]. As various poisons coexist in the flue gas, resistance to more than one kind of poison is quite urgent to explore, and SCR catalysts with superior resistance to different poisons are required.

\* Corresponding author at: Key Laboratory of Environment Remediation and Ecological Health, Ministry of Education, College of Environmental & Resources Science, Zhejiang University, Hangzhou 310058, PR China.

E-mail addresses: [haiqiangwang@zju.edu.cn](mailto:haiqiangwang@zju.edu.cn), [anghaiqiang2008@126.com](mailto:wanghaiqiang2008@126.com) (H. Wang).

Based on the deactivation mechanism related to alkali/alkaline metals, phosphorus compounds and lead, abundant acidic sites, strong redox ability and special protection structure are the essential properties for catalysts. Ceria, which always acts as a very active oxide in the SCR reaction, possesses considerable oxygen storage capacity owing to the redox cycling between  $\text{Ce}^{3+}$  and  $\text{Ce}^{4+}$  [8,22–25]. Moreover, the SCR performance of ceria-based catalysts can be remarkably enhanced by introducing solid acid components such as tungsta, niobia, and sulfate, which is mainly due to their excellent redox ability and strong acidity [26,27]. Furthermore, it has been reported that the addition of  $\text{Nb}_2\text{O}_5$  not only promote the acidity of catalysts but also redox ability [26–29]. Our previous work also claimed that the utilization of “core-shell” materials is proven to be a useful method to improve the alkali metal resistance of SCR catalysts [25,30–32].

Thus, in this work, we synthesize a novel ceria nanotubes material as the “shell” supporting material and dope with niobia as the “core” phase to investigate its SCR activity and resistance against potassium, phosphorus, and lead. Aiming to observe the effect of nanotubular structure on ceria materials, we also prepare  $\text{CeO}_2$  nanoparticles and dope with niobia as a reference sample. The “core-shell”  $\text{Ce-Nb}$  material demonstrates remarkable  $\text{NO}_x$  conversion and superior resistance to K, P, and Pb compared to the nanoparticle material. A series of characterizations, i.e. X-ray diffraction (XRD), transmission electron microscopy (TEM), high-resolution TEM (HR-TEM), Brunauer-Emmet-Teller (BET) surface area analysis, X-ray photoelectron spectroscopy (XPS),  $\text{H}_2$  temperature-programmed reduction ( $\text{H}_2\text{-TPR}$ ) and  $\text{NH}_3$  adsorption Fourier-transform infrared spectroscopy ( $\text{NH}_3\text{-FTIR}$ ), are conducted to investigate the mechanism behind the enhanced resistance. The described combination of niobia with ceria nanotubes support provides a new strategy for the design of SCR catalysts with excellent resistance to different kinds of poisons.

## 2. Experimental

### 2.1. Catalyst preparation

The support, ceria nanotubes, are synthesized with P123 as template agent and  $\text{CeCl}_3\cdot 7\text{H}_2\text{O}$  as cerium precursor by a typical hydrothermal method reported in the literature [33]. Firstly, certain amount of P123 and  $\text{CeCl}_3\cdot 7\text{H}_2\text{O}$  with a molar ratio of  $n(\text{P123}) : n(\text{CeCl}_3\cdot 7\text{H}_2\text{O}) = 1:5$  are added into a 40 mL mixed solution of water and ethanol (with a ratio of water: ethanol = 1:1). The mixture is stirred at room temperature for 30 min then  $\text{NH}_3\text{H}_2\text{O}$  is added dropwise until the pH reached 9–10 and a red flocculent precipitate is produced. After continuous stirring for a short time, the precipitate is transferred into a 100 mL stainless steel autoclave and keep at 160 °C for 72 h. After hydrothermal treatment, the precipitate is first washed with deionized water and then with ethanol to remove the template agent. After drying at 60 °C overnight, the ceria nanotubes (yellow powder) are prepared and named as CeNTs.

Another particle support with uniform particle size is also prepared as a control to research the influence of nanotubular structure on titanate nanotubes in this work [34]. The  $\text{CeO}_2$  nanoparticles are prepared by dissolving 2.74 g  $(\text{NH}_4)_2\text{Ce}(\text{NO}_3)_6$  and 10 g  $\text{CH}_3\text{COONa}$  into 70 mL deionized water and then adding 10 mL ethanol into the solution. After stirring at room temperature for 1 h, the mixture is transferred into a 100 mL stainless steel autoclave and keep at 220 °C for 12 h. Then, yellow precipitate is collected by centrifugation and washes with deionized water and ethanol. Finally, the precipitate is dried at 60 °C overnight and named as  $\text{CeO}_2(\text{N})$ . The synthesis procedure of ceria nanotubes and ceria nanoparticles are shown as follows in **Scheme 1**.

The introduction of niobium oxide (mass ratio is 5 wt %) into the ceria nanotubes and nanoparticles is carried out by impregnating the cerium support with the required amount of  $\text{C}_{10}\text{H}_5\text{NbO}_{20}\cdot x\text{H}_2\text{O}$  aqueous solution [26,27,29]. The mixture is then stirred for 6 h, dried at 80 °C overnight, and calcined at 450 °C for 3 h. The niobia supported catalysts are referred to as Nb-CeNTs and Nb- $\text{CeO}_2(\text{N})$ , respectively.

Alkali metal, phosphate, and heavy metal poisons are separately added by impregnating the catalysts into  $\text{KNO}_3$ ,  $(\text{NH}_4)\text{H}_2\text{PO}_4$ , and  $\text{Pb}(\text{NO}_3)_2$  solutions with a certain amount of potassium, phosphate, and lead [7,10–12,35,36]. Based on the literature, the mass ratios of potassium oxide, phosphorus oxide and lead oxide are 1, 5, and 4 wt %, respectively. Then, the mixed solution is continuously stirred for 6 h, dried at 80 °C overnight, and calcined at 450 °C for 3 h. The catalysts poisoned with potassium, phosphate, and lead are labeled as K/Nb-CeNTs, P/Nb-CeNTs, Pb/Nb-CeNTs and K/Nb- $\text{CeO}_2(\text{N})$ , P/Nb- $\text{CeO}_2(\text{N})$ , Pb/Nb- $\text{CeO}_2(\text{N})$ , respectively.

### 2.2. Catalyst characterization

The crystal phases of samples are obtained by XRD with  $\text{Cu K}\alpha$  radiation (model D/max RA, Rigaku Co., Japan). The data are collected through scattering angles ( $2\theta$ ) ranging from 5° to 80° with a step size of 0.02°. Microscopic morphology, structure, and the distribution of the active phase are detected by TEM (JEM-2010, Japan). The specific surface areas, pore volume and pore size of samples are obtained by a nitrogen adsorption apparatus (JW-BK132F, China) with the BET method. All the catalysts are pre-treated before measurement at 100 °C under vacuum. Data are obtained at a relative pressure ( $P/P_0$ ) ranging between 0.05 and 0.30. The surface properties and valence state distribution are investigated by XPS with  $\text{Al K}\alpha$  X-ray ( $h\nu = 1486.6$  eV) radiation operated at 150 W (Thermo ESCALAB 250, USA).  $\text{H}_2\text{-TPR}$  is carried on a thermal conductivity detector instrument (TP-5079) with 50 mg of catalyst. Prior to the experiments, catalysts are pre-treated under pure He at 300 °C for 1 h. The reduction process is conducted through heating the samples in  $\text{H}_2$  atmosphere (6%  $\text{H}_2/\text{N}_2$ ) at a flow rate of 30 mL/min. The heating rate is 10 °C/min, and a preheat treatment at 100 °C for 60 min is necessary before raising the temperature. The type of acid sites for the samples are studied through  $\text{NH}_3$  adsorption FTIR experiments on an FT-IR spectrophotometer (Tensor 27, Bruker). All the samples are pre-treated at 350 °C with purified  $\text{N}_2$ , and then the catalysts are exposed to 1000 ppm anhydrous  $\text{NH}_3$  at 100 °C for about 30 min. The spectra are recorded after evacuating the samples for 30 min at 100 °C.

### 2.3. SCR activity tests and measurements

Selective catalytic reduction of  $\text{NO}_x$  with  $\text{NH}_3$  is carried out in a fixed-bed quartz reactor (1 cm i.d.). A type K thermocouple is placed at the centre of the bed for temperature measurements. The experiments are performed under atmospheric pressure at 150–500 °C with 0.5 g of 40–60 mesh catalyst. The typical gas composition is 600 ppm  $\text{NH}_3$ , 600 ppm  $\text{NO}$ , 3.5%  $\text{O}_2$ , 5%  $\text{H}_2\text{O}$ , and balance  $\text{N}_2$ . The gas hourly space velocity (GHSV) is calculated as follows:

$$\text{GHSV} (\text{h}^{-1}) = \text{Total gases flow rate/Catalyst volume} \quad (1)$$

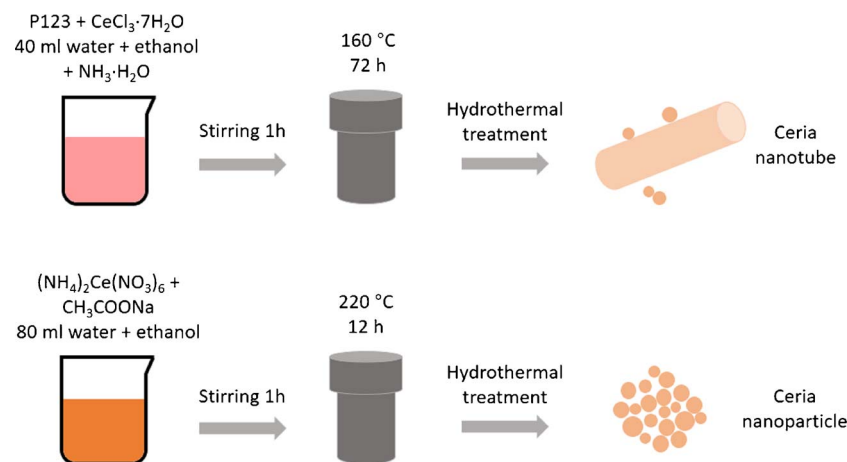
The total gases flow rate in the experiments is 2 L/min under normal temperature and pressure. The pressure is kept the same during the test and the gases flow rate is changeless when temperature varies from 150 °C to 500 °C. The catalyst volume is about 1.2  $\text{cm}^3$ . Thus, the calculated GHSV herein is kept at approximately 100,000  $\text{h}^{-1}$ .

$\text{NO}$ ,  $\text{NO}_2$ , and  $\text{O}_2$  concentrations are detected by a flue gas analyser (Testo 350, Testo Inc., Germany). The concentration of  $\text{N}_2\text{O}$  is monitored by another flue gas analyser (G200, Geotech, UK).  $\text{NO}_x$  conversion and  $\text{N}_2$  selectivity are calculated using the following equations [37,38]:

$$\text{NO}_x \text{ conversion \%} = ([\text{NO}_x]_{\text{in}} - [\text{NO}_x]_{\text{out}}) / [\text{NO}_x]_{\text{in}} \times 100\% \quad (2)$$

$$\text{N}_2 \text{ selectivity \%} = ([\text{NO}_x]_{\text{in}} + [\text{NH}_3]_{\text{in}} - [\text{NO}_x]_{\text{out}} - [\text{NH}_3]_{\text{out}} - 2[\text{N}_2\text{O}]) / ([\text{NO}_x]_{\text{in}} + [\text{NH}_3]_{\text{in}} - [\text{NO}_x]_{\text{out}} - [\text{NH}_3]_{\text{out}}) \times 100\% \quad (3)$$

where  $[\text{NO}_x] = [\text{NO}] + [\text{NO}_2]$ , and the subscripts in and out represent the inlet and outlet concentration of  $\text{NO}_x$  at steady state, respectively.



**Scheme 1.** Schematic illustration of the synthesis procedure of ceria nanotubes and ceria nanoparticles.

### 3. Results and discussion

#### 3.1. SCR performance and resistance to different poisons (K, P, Pb)

As a novel active phase, niobia is successfully loaded on two different kinds of carriers, ceria nanotubes and  $\text{CeO}_2$  nanoparticles. The SCR performance and differentiated resistance against potassium, phosphorus, and lead are shown in Fig. 1. As ceria is always used as the active phase in SCR catalysts, the carrier of CeNTs is also tested in the SCR system with the results shown in Fig. 1(a). The CeNTs exhibits good reduction efficiency with the highest  $\text{NO}_x$  conversion of 85% at 350 °C, approximately. However, the reduction rate shows a rapid decline as the temperature increased. When doping niobia on CeNTs, the Nb-CeNTs catalyst possesses superior SCR performance. It is demonstrated that the addition of niobium species do promote the reduction efficiency. Besides, even though both Nb-CeNTs and Nb- $\text{CeO}_2$ (N) catalysts yield excellent  $\text{NO}_x$  removal performance, Nb-CeNTs shows superior SCR activity where the  $\text{NO}_x$  conversion exceeds 90% in the temperature region of 275–450 °C. As for Nb- $\text{CeO}_2$ (N), the highest  $\text{NO}_x$  removal rate is 90%, which is achieved at 350 °C. This result indicates that ceria nanotubes is really a better carrier for niobium oxide than  $\text{CeO}_2$  nanoparticles in the SCR reaction. In addition, the  $\text{SO}_2$  and  $\text{H}_2\text{O}$  resistibility performance of CeNTs and Nb-CeNTs are also tested with a higher GHSV of about 200,000  $\text{h}^{-1}$ . As shown in Fig. S1, after  $\text{SO}_2$  and  $\text{H}_2\text{O}$  are introduced into the system for 20 h, the  $\text{NO}_x$  conversion of CeNTs declines from 74% to 40%, while that of Nb-CeNTs catalyst only

has a negligible change of ~5%. These results indicate that the addition of niobia helps to improve the  $\text{SO}_2$  and  $\text{H}_2\text{O}$  resistance of CeNTs.

After exposing the fresh catalysts to different kinds of poisons, these two catalysts exhibit obviously different resistance performance. It is observed that Nb-CeNTs expresses relatively satisfactory resistance to potassium, phosphorus, and lead, except that the alkali resistance is a little bit inferior to the catalysts we proposed in our previous work [30–32]. Furthermore, the resistance of Nb-CeNTs against phosphorus is much better, as the  $\text{NO}_x$  conversion is above 85% in the temperature region of 300–400 °C. Since the SCR performance almost stays the same with the fresh catalyst after the addition of lead except a little bit decline of activity in the low temperature range, the Nb-CeNTs is verified to have superior resistance to lead. However, the Nb- $\text{CeO}_2$ (N) catalyst shows much inferior  $\text{NO}_x$  reduction ability with the introduction of poisons, and only phosphorus shows slight damage to the Nb- $\text{CeO}_2$ (N) catalyst. After the addition of potassium and lead, the  $\text{NO}_x$  removal rate decreases below 35%, and the highest activity of Pb/Nb- $\text{CeO}_2$ (N) is only ~20%.

In addition, the  $\text{N}_2$  selectivity and  $\text{N}_2\text{O}$  production for all the catalysts are shown in the Supplementary Information (Fig. S3 and Fig. S4). The  $\text{N}_2$  selectivity of Nb-CeNTs and the poisoned catalysts are all above 95% except that of K/Nb-CeNTs is about 90% at 450 °C. Moreover, the  $\text{N}_2\text{O}$  generates in the whole temperature window for each catalyst is below 15 ppm (see Fig. S3). However, despite Nb- $\text{CeO}_2$ (N) and P/Nb- $\text{CeO}_2$ (N) showing high  $\text{N}_2$  selectivity and low  $\text{N}_2\text{O}$  concentrations, the  $\text{N}_2$  selectivity performance of K/Nb- $\text{CeO}_2$ (N) and Pb/Nb- $\text{CeO}_2$ (N)

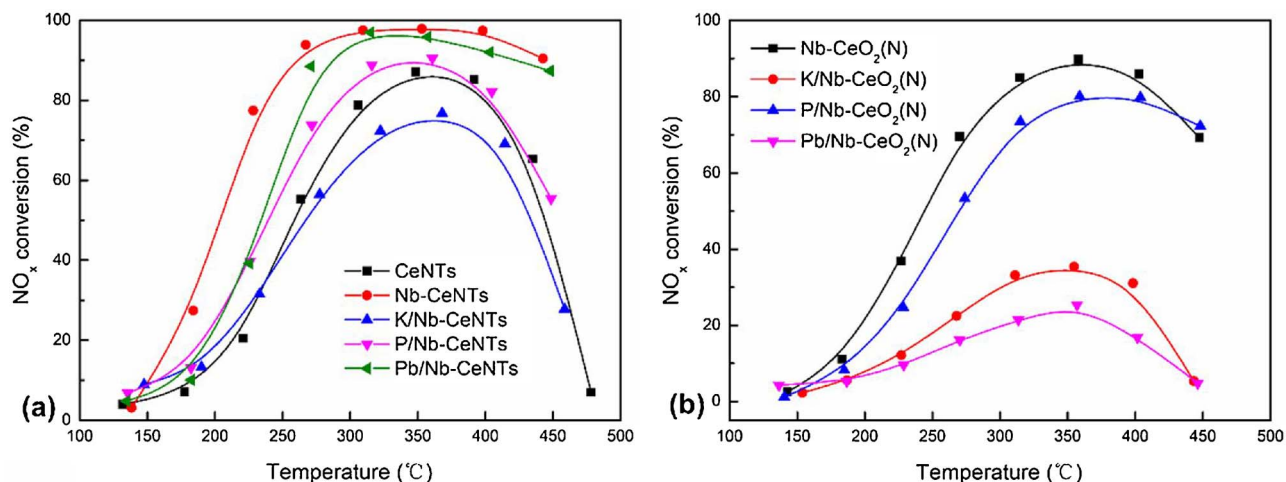


**Fig. 1.**  $\text{NO}_x$  conversion of the Nb-CeNTs and Nb-CeO<sub>2</sub>(N) catalysts and that after K, P, Pb doping. Reaction conditions:  $[\text{NO}] = [\text{NH}_3] = 600 \text{ ppm}$ ,  $[\text{O}_2] = 3.5\%$ ,  $[\text{H}_2\text{O}] = 5\%$ , balance  $\text{N}_2$ , catalyst 0.5 g, and GHSV about 100,000  $\text{h}^{-1}$ .

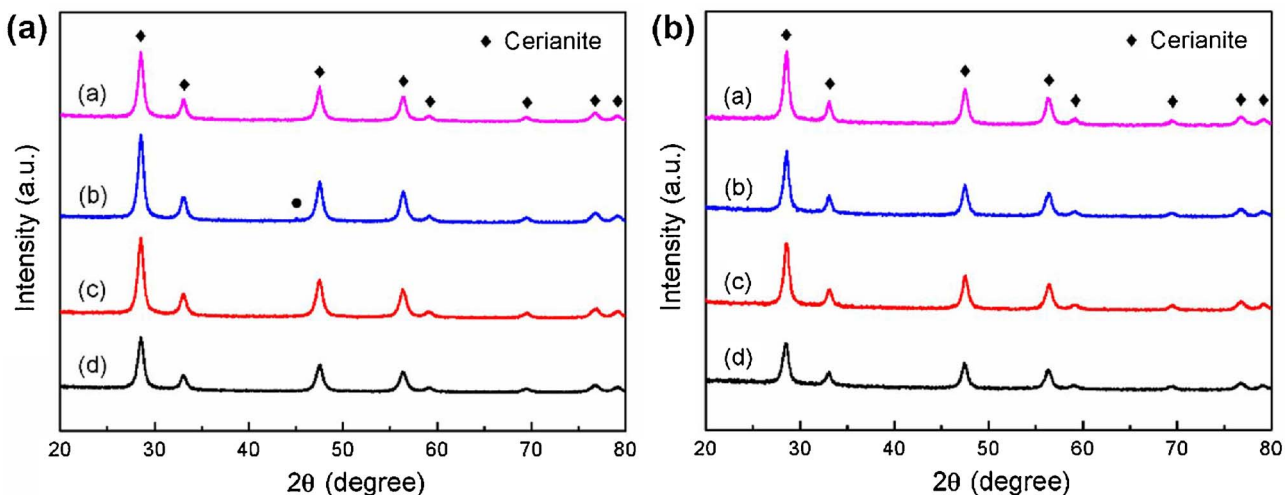


Fig. 2. Powder XRD patterns of (a): Nb-CeNTs (a), P/Nb-CeNTs (b), K/Nb-CeNTs (c), Pb/Nb-CeNTs (d); (b): Nb-CeO<sub>2</sub>(N) (a), P/Nb-CeO<sub>2</sub>(N) (b), K/Nb-CeO<sub>2</sub>(N) (c), Pb/Nb-CeO<sub>2</sub>(N) (d).

decrease sharply when the temperature exceeds 350 °C, which is accompanied with a large mass of N<sub>2</sub>O (see Fig. S4). The obviously different resistance performance between Nb-CeNTs and Nb-CeO<sub>2</sub>(N) affirms that the nanotubular structure can prevent the catalyst poisoning especially by potassium and lead. Thus, the novel Nb-CeNTs catalyst should be a promising substitute for the commercial VWT catalyst in the application of SCR technology. The promotion mechanism is discussed in detail below.

### 3.2. Morphology and structure investigation

The crystal phases of all catalysts are characterized by XRD, and the results are shown in Fig. 2. Cerianite is clearly the main crystal phase of both Nb-CeNTs and Nb-CeO<sub>2</sub>(N), with characteristic reflections generating at 28.55°, 33.08°, 47.47°, 56.33°, 59.08°, 69.40°, 76.69°, and 79.06° (PDF#34-0394). The niobium species may be mainly present as an amorphous state or disperse very well on the supports of CeNTs and CeO<sub>2</sub>(N) as there is no obvious characteristic reflection corresponding to niobium species being detected. After the addition of poisons into the fresh catalysts, the crystal phases barely change, but the intensity of characteristic reflections varies. As compared with Nb-CeNTs, the peak intensity of P/Nb-CeNTs increases, and a new weak characteristic reflection appears at 45.06°, which is related to hydrogen niobium phosphate hydroxide hydrate (PDF#47-0151). This reveals that phosphorus can accelerate the crystallization of cerianite and may prefer to bond to the active phase, niobium oxide. As for K/Nb-CeNTs and Pb/Nb-CeNTs, the crystal phases have not changed, but the intensity of the characteristic reflections increases a little for K/Nb-CeNTs and declines a little for Pb/Nb-CeNTs. It is demonstrated that potassium also facilitates the crystallization of cerianite in CeNTs, while lead have slight effect on the structure of CeNTs. In addition, the crystal phases and crystallinity of K/Nb-CeO<sub>2</sub>(N) and P/Nb-CeO<sub>2</sub>(N) barely change when compared to Nb-CeO<sub>2</sub>(N). However, with the introduction of lead into Nb-CeO<sub>2</sub>(N), the peak intensity also decreases, which is similar to Pb/Nb-CeNTs and suggests that lead produces side effects on the structure of cerium carriers.

Fig. 3 shows the TEM and HR-TEM images of fresh and poisoned CeNTs supported catalysts. As clearly shown in Fig. 3(a), the ceria nanotubes possess a nanotubular structure with individual nanotubes being well separated. Furthermore, the length varies from hundred nanometres to several micrometres, and the outer diameter varies from 20 nm to 50 nm. There are some nanoparticles attaching on the nanotubes or clustering together. With a further increase of the magnification, the nanoparticles are verified to be cerium oxides in Fig. 3(b). The lattice spacing is measured at ~0.312 nm and attributed to the (111)

and (111) planes of cerianite (PDF#34-0394). After depositing niobia on ceria nanotubes, the morphology remains unchanged except that more nanoparticles are observed on the nanotubes. A square area labelled in red in Fig. 3(c) is selected to further check the crystal structure. The result shown in Fig. 3(d) reveals that the lattice spacing is measured at ~0.278 nm, which is corresponding to the (314) plane of Nb<sub>2</sub>O<sub>5</sub> (PDF#-19-0862), indicating the niobium species are successfully deposited on CeNTs and present as Nb<sub>2</sub>O<sub>5</sub>. After exposure to different poisons, the nanotubular structure of K/Nb-CeNTs, P/Nb-CeNTs and Pb/Nb-CeNTs are still maintained except that the nanotubes in Pb/Nb-CeNTs show some aggregation, which is in good agreement with the XRD results mentioned above. As the SCR performance results show that the Nb-CeNTs owns best resistance against lead, the slight aggregation of ceria nanotubes may not be the main factor for the deactivation of these catalysts.

The TEM images in Fig. 4(a) show the morphology of prepared CeO<sub>2</sub> nanoparticles. The particles are clearly nanocubes with a size in the range of 4–11 nm, and the major size is 7–8 nm (Fig. 4(b)). The obtained CeO<sub>2</sub> nanoparticles in this work have a similar particle size with the ceria in ceria nanotubes as shown in Fig. 3(a) and (b). Thus, the CeNTs and CeO<sub>2</sub>(N) can be used to study the role of nanotubes in the enhanced resistance to potassium, phosphorus, and lead without the effect of particle size. With the introduction of niobia into CeO<sub>2</sub>(N), the morphology and particle size of Nb-CeO<sub>2</sub>(N) barely change, and the lattice spacing shown in Fig. 4(b) is measured at 0.312 nm from the (111) plane of cerianite (PDF#34-0394). To confirm whether the niobium species are supported on CeO<sub>2</sub>(N) or not, a square area lined in red in Fig. 4(c) is selected to conduct an energy dispersive X-ray (EDX) mapping experiment. The results show that the weight proportion of Nb is 4.6%, which is a little bit lower than the theoretical ratio in experimental section. Therefore, most of the niobium species are successfully introduced and disperse well. Moreover, after the addition of poisons, the morphology and particle size of K/Nb-CeO<sub>2</sub>(N) and Pb/Nb-CeO<sub>2</sub>(N) remain almost the same as Nb-CeO<sub>2</sub>(N), but P/Nb-CeO<sub>2</sub>(N) shows a serious aggregation of the nanoparticles. Since the Nb-CeO<sub>2</sub>(N) catalyst achieves a superior resistance against phosphorus and the SCR performance of K/Nb-CeO<sub>2</sub>(N) and Pb/Nb-CeO<sub>2</sub>(N) are both inferior, the slight change in micro-structure is not the most important factor for the resistance of Nb-CeO<sub>2</sub>(N) catalyst against potassium, phosphorus, and lead.

Besides, XPS etching characterization is conducted to further evaluate the location of Nb species in Nb-CeNTs and Nb-CeO<sub>2</sub>(N). Since the penetration depth of XPS is about 2–3 nm, only Nb species on the outside of CeNTs and on the surface of CeO<sub>2</sub>(N) can be detected. Thus, when the samples are etched via ion sputtering to cut the wall of the

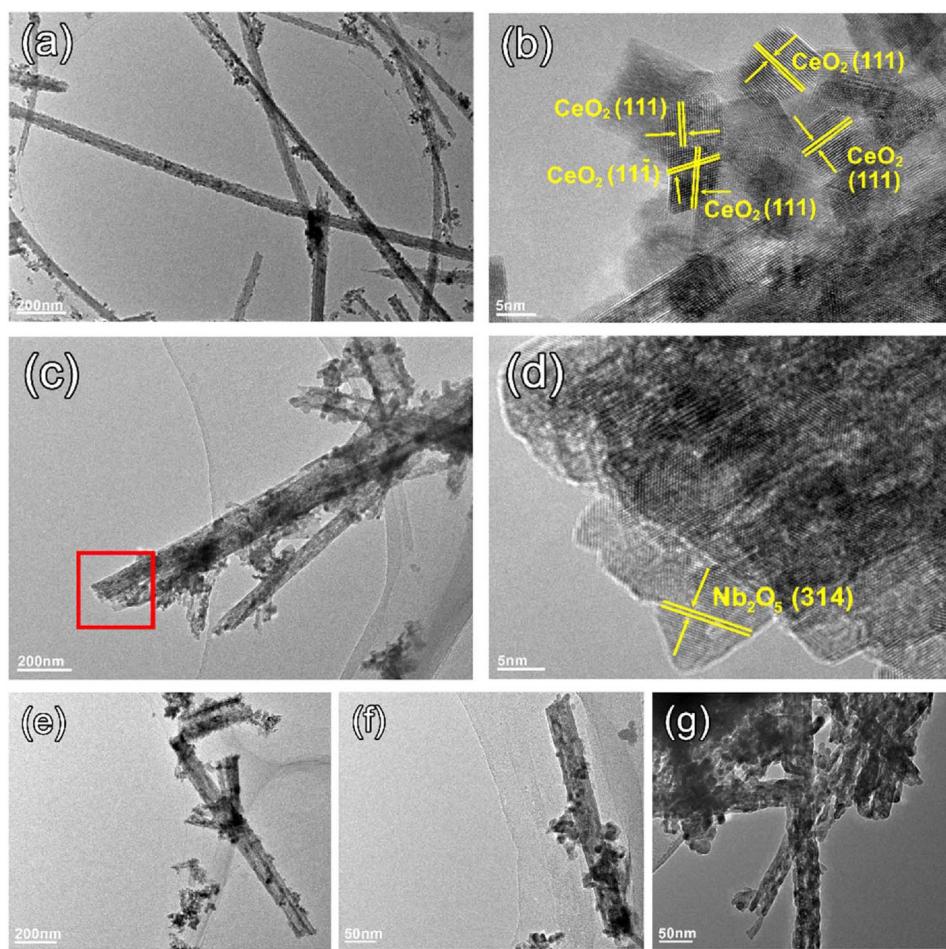


Fig. 3. TEM and HR-TEM images of CeNTs (a), (b); Nb-CeNTs (c), (d); K/Nb-CeNTs (e), P/Nb-CeNTs (f), Pb/Nb-CeNTs (g).

CeNTs, Nb species inside CeNTs will be exposed. For the sample of niobia located only on the surface of the supports (e.g., Nb-CeO<sub>2</sub>(N)), the Nb content will decrease during the ion etching treatment process. While for the sample of niobia located inside the CeNTs, the etching will lead to enlarged exposure of Nb species, resulting in an increase of Nb content. In consequence, the XPS results confirm this conjecture (Table 1). In addition, the etching treatment is operated with a rate of 1 nm/10 s and the thickness of CeNTs is about 20–50 nm. Thus after 500 s ion etching, the detected Nb content is the Nb species on the other side of CeNTs and shows a slight decline, indicating that most of niobia species are indeed located inside CeNTs. For the Nb-CeO<sub>2</sub>(N) sample, the particle size of CeO<sub>2</sub>(N) is about 4–11 nm. After 200 s ion etching, the slight increased Nb content reveals that it is derived from the Nb species deposited on the surface of another CeO<sub>2</sub>(N) particle, demonstrating that most of the niobia species are located on the surface of the CeO<sub>2</sub>(N) nanoparticles.

To further investigate the physical characteristics of the fresh and poisoned catalysts, the specific surface area, pore volume, and pore size are studied by nitrogen adsorption-desorption experiments with the results shown in Table 2. It is observed that the surface areas of CeNTs and CeO<sub>2</sub>(N) are quite close and that of CeO<sub>2</sub>(N) is even higher, further eliminating the influence of surface area on the SCR performance and resistance against different poisons. For CeNTs, the pore volume mainly results from the internal volume inside ceria nanotubes and the interstices between nanotubes. The pore size corresponds to the inner diameter of ceria nanotubes and the interstice width between nanotubes. When niobium oxide deposited on the CeNTs, the surface area barely increases, but the pore volume and pore size both decrease slightly. This reveals that the niobium oxide are mainly introduced into the

nanotubes internally thus have no influence on the surface area but affect the pore volume and size of the ceria nanotubes. After further addition of poisons into the Nb-CeNTs, the surface area of K/Nb-CeNTs, P/Nb-CeNTs and Pb/Nb-CeNTs all decrease, which is mainly caused by the coverage of poison species and change in the structure of the ceria nanotubes. The surface area even declines from 55.0 m<sup>2</sup>/g to 44.4 m<sup>2</sup>/g for Pb/Nb-CeO<sub>2</sub>(N), primarily resulting from the aggregation of nanotubes shown in the TEM images. However, the pore volume and pore size of poisoned catalysts all increase compared with those of Nb-CeNTs, probably indicating that the poisons all deposited on the outside of the ceria nanotubes and thus exhibit little effect on the internal volume and pore diameter. Moreover, the increase of pore volume and size can be derived from the interstices between nanotubes. As for the nanoparticle CeO<sub>2</sub>(N) samples, the pore volume mainly arises from the interstices between particles, and the pore size is determined by the interstices width, which always increases with the diameter of the composites. As the particle size of CeO<sub>2</sub>(N) is verified to vary from 4 nm to 11 nm, the pore size is calculated to be approximately 4.10 nm. After adding the active phase, the surface area and pore volume of Nb-CeO<sub>2</sub>(N) both decrease, but the pore size increases slightly. It can be concluded that the deposition of niobium species covers part of the CeO<sub>2</sub>(N) surface, plugs the interstices, and enlarges the particles. With the introduction of K, P and Pb, the surface area of poisoned catalysts all decrease, pore size increases slightly and pore volume almost remains the same as Nb-CeO<sub>2</sub>(N). Among the obvious changes in the surface area, the P/Nb-CeO<sub>2</sub>(N) samples reveal the sharpest decline, from 62.5 m<sup>2</sup>/g to 45.6 m<sup>2</sup>/g, agreeing well with the results of TEM images. Although the CeNTs and CeO<sub>2</sub>(N) based catalysts have similar physical characteristics with each other, the SCR performance,

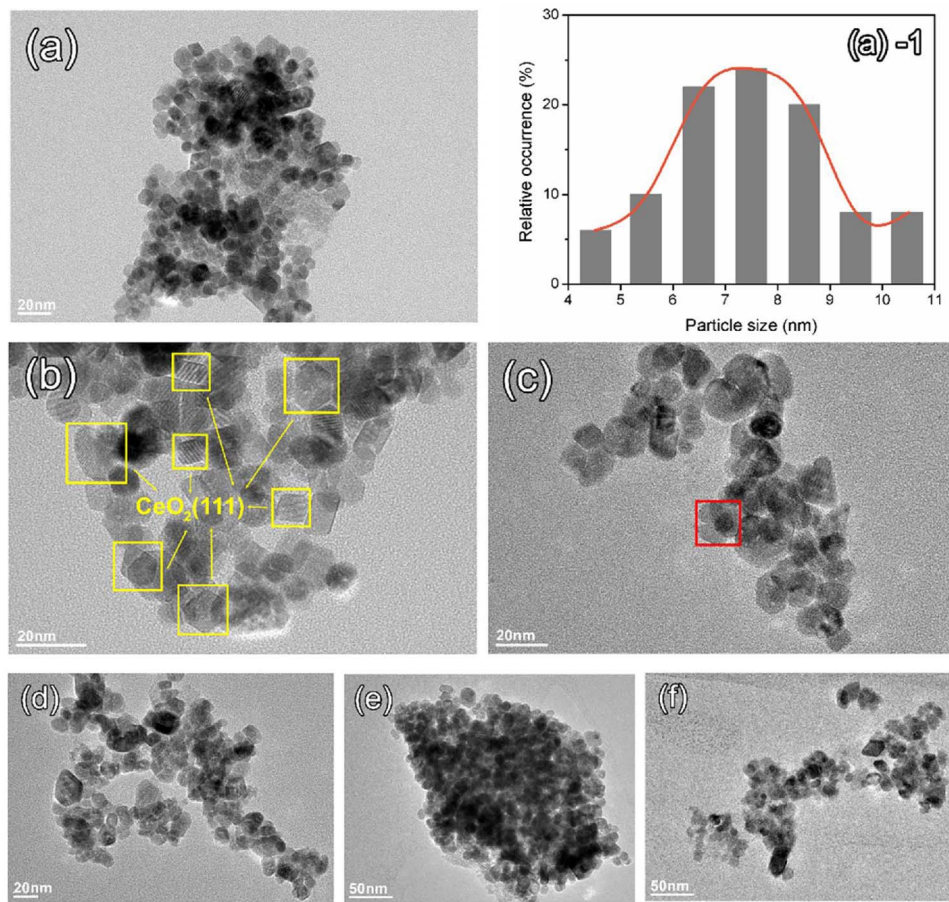


Fig. 4. TEM and HR-TEM images of  $\text{CeO}_2(\text{N})$  (a), (b);  $\text{Nb}-\text{CeO}_2(\text{N})$  (c);  $\text{K}/\text{Nb}-\text{CeO}_2(\text{N})$  (d);  $\text{P}/\text{Nb}-\text{CeO}_2(\text{N})$  (e),  $\text{Pb}/\text{Nb}-\text{CeO}_2(\text{N})$  (f).

**Table 1**  
Atomic concentration with XPS characterization.

Catalyst	Treatment	Ce (at. %)	Nb (at. %)	O (at. %)
Nb-CeNTs	Before etching	20.71	5.97	64.70
	100s etching	24.67	6.16	65.14
	200s etching	25.72	6.31	64.67
	300s etching	26.75	6.49	64.11
	400s etching	27.16	6.49	63.89
	500s etching	26.97	6.45	63.79
Nb- $\text{CeO}_2(\text{N})$	Before etching	21.73	5.58	64.63
	100s etching	24.82	5.54	67.14
	200s etching	26.63	5.48	67.89
	300s etching	26.32	5.51	68.17
	400s etching	27.09	5.52	67.29
	500s etching	27.02	5.48	67.20

**Table 2**  
The physical characteristics of the samples.

Catalysts	BET surface area ( $\text{m}^2/\text{g}$ )	Pore volume ( $\text{cm}^3/\text{g}$ )	Pore size (nm)
CeNTs	53.9	0.17	6.91
Nb-CeNTs	55.0	0.15	6.84
K/Nb-CeNTs	52.7	0.20	8.91
P/Nb-CeNTs	50.8	0.21	8.52
Pb/Nb-CeNTs	44.4	0.19	8.62
$\text{CeO}_2(\text{N})$	66.3	0.10	4.10
Nb- $\text{CeO}_2(\text{N})$	62.5	0.06	4.42
K/Nb- $\text{CeO}_2(\text{N})$	56.8	0.06	4.52
P/Nb- $\text{CeO}_2(\text{N})$	45.6	0.06	4.67
Pb/Nb- $\text{CeO}_2(\text{N})$	56.0	0.07	4.59

especially resistance to K and Pb, are quite different. The surface area, which is confirmed to be beneficial to the adsorption of reactants, is not the most crucial factor, but the nanotubular structure of ceria nanotubes plays an important role for the  $\text{NO}_x$  conversion and resistance performance in this work.

### 3.3. Surface valence and redox properties

The surface atomic proportions and chemical valence distributions are investigated by XPS, with the Nb 3d spectra shown in Fig. 5, Ce 3d spectra in Fig. 6, and O 1s spectra in Fig. 7. The presence of lower valence in metal oxides, i.e.  $\text{Nb}^{4+}$  species in  $\text{Nb}_2\text{O}_5$ , is reported to be always accompanied by oxygen defects [26,28]. The presence of oxygen defects can promote the adsorption of chemisorbed oxygen on the catalyst surface and accelerate the  $\text{Nb}^{5+}/\text{Nb}^{4+}$  redox cycles. On the contrary, if the  $\text{Nb}^{4+}$  species decrease or disappear, the  $\text{Nb}^{5+}/\text{Nb}^{4+}$  redox cycles will be seriously restrained, thus significantly affecting the redox properties of the catalysts [26,28]. Hence, to precisely calculate the  $\text{Nb}^{4+}/\text{Nb}^{4+} + \text{Nb}^{5+}$  ratio, the raw Nb 3d spectra in Fig. 5(a) for CeNTs samples and those in Fig. 5(b) for  $\text{CeO}_2(\text{N})$  samples are all deconvoluted into several overlapping individual peaks. The green-labelled peaks at 205.3 and 208.0 eV correspond to the Nb 3d  $5/2$  and Nb 3d  $3/2$  transitions of  $\text{Nb}^{4+}$ , respectively, while the blue-labelled ones at 206.8 and 209.6 eV represent the Nb 3d  $5/2$  and Nb 3d  $3/2$  transitions of  $\text{Nb}^{5+}$ , respectively [26,28,39]. The atomic proportions are calculated based on the corresponding peak areas of  $\text{Nb}^{4+}$  and  $\text{Nb}^{5+}$ , with the results shown in Table 3. The Nb-CeNTs (32.6%) catalyst is found to be more  $\text{Nb}^{4+}$ -rich than  $\text{Nb}-\text{CeO}_2(\text{N})$  (29.9%), revealing the chemical redox property of the active niobium species may be tuned by the ceria nanotubes. Thus, more  $\text{Nb}^{4+}$  species accompany with oxygen defects

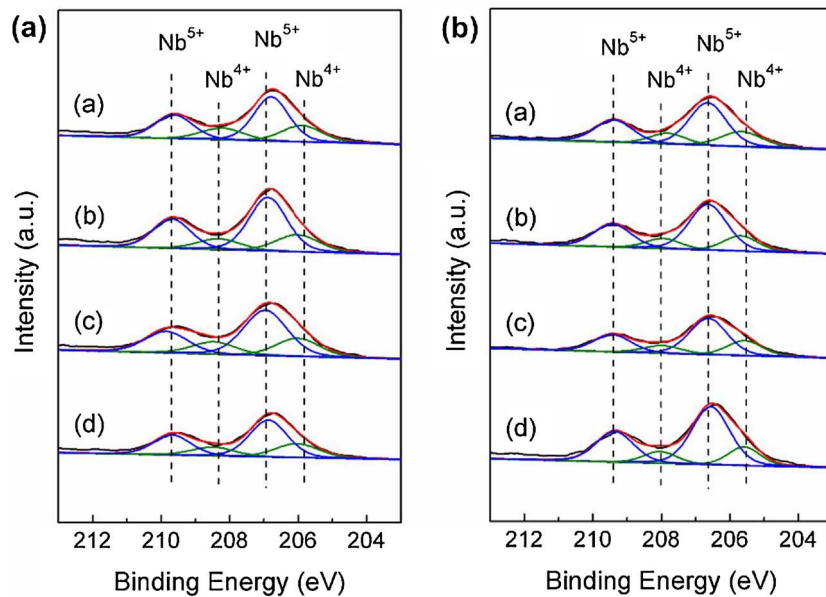


Fig. 5. XPS spectra of Nb 3d (a): Nb-CeNTs (a), K/Nb-CeNTs (b), P/Nb-CeNTs (c), Pb/Nb-CeNTs (d); (b): Nb-CeO<sub>2</sub>(N) (a), K/Nb-CeO<sub>2</sub>(N) (b), P/Nb-CeO<sub>2</sub>(N) (c), Pb/Nb-CeO<sub>2</sub>(N) (d).

promote the NO<sub>x</sub> reduction rate. For catalysts poisoned by K, P, and Pb, the amount of Nb<sup>4+</sup> in P/Nb-CeNTs and Pb/Nb-CeNTs decrease slightly to 31.2% and 31.4%, respectively. However, the Nb<sup>4+</sup> content of K/Nb-CeNTs sample declines from 32.6% to 27.9%. This sequence of Nb<sup>4+</sup> amounts is in good agreement with the SCR performance of these catalysts, indicating that the redox property is an important factor for the CeNTs catalysts. Beyond that, the K/Nb-CeO<sub>2</sub>(N) and Pb/Nb-CeO<sub>2</sub>(N) catalysts that have poor capacity to reduce NO<sub>x</sub> also show obvious decline of Nb<sup>4+</sup> content compared with Nb-CeO<sub>2</sub>(N), whereas P/Nb-CeO<sub>2</sub>(N) still has more Nb<sup>4+</sup> species than K/Nb-CeO<sub>2</sub>(N) and Pb/Nb-CeO<sub>2</sub>(N). Thus, the smooth Nb<sup>5+</sup>/Nb<sup>4+</sup> redox cycles play an important role in the SCR reaction for CeNTs and CeO<sub>2</sub>(N) supported catalysts. As the active Nb<sub>2</sub>O<sub>5</sub> is mostly confined inside the ceria nanotubes, the addition of poisons has little effect on the Nb<sup>4+</sup> content, making Nb<sub>2</sub>O<sub>5</sub> being immune to the attack of potassium, phosphate, and lead than that loading on CeO<sub>2</sub>(N) and thus achieving superior resistance.

As the ceria always acts as a part of active phase, the valence

distribution of cerium species is also investigated, and the Ce 3d spectra in Fig. 6 are also deconvoluted into several overlapping peaks. The peaks centre at 901.3, 907.3, 916.9, 882.7, 888.7 and 898.3 eV that labelled in grey represent the 3d<sup>10</sup>4f<sup>0</sup> state of Ce<sup>4+</sup>, while the peaks at 903.4 and 885.2 eV that labelled in pink represent the 3d<sup>10</sup>4f<sup>1</sup> initial electronic state corresponding to Ce<sup>3+</sup> [40,41]. It also has been widely reported that the Ce<sup>3+</sup> generally originates from ceria defects and is always accompanied with the formation of oxygen vacancies [42–44]. The presence of Ce<sup>3+</sup> species and oxygen vacancies will create a charge imbalance and unsaturated chemical bonds, leading to an increase of chemisorbed oxygen species on the catalyst surface and hence promoting the repeatable Ce<sup>4+</sup>/Ce<sup>3+</sup> redox cycles [42,44,45]. On the contrary, the Ce<sup>4+</sup>/Ce<sup>3+</sup> redox cycles will be seriously restrained once Ce<sup>3+</sup> disappears [44], which is quite similar to the Nb<sup>5+</sup>/Nb<sup>4+</sup> redox cycles. According to the deconvolution spectra, the proportions of Ce<sup>3+</sup>/Ce<sup>3+</sup> + Ce<sup>4+</sup> can be calculated, and the results are shown in Table 3. Interestingly, the Ce<sup>3+</sup> proportion in Nb-CeNTs and Nb-

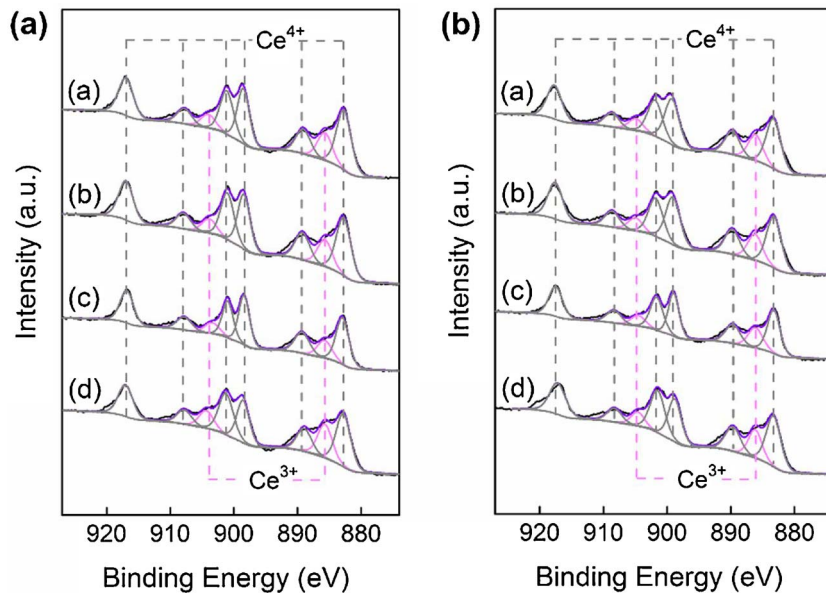


Fig. 6. XPS spectra of Ce 3d (a): Nb-CeNTs (a), K/Nb-CeNTs (b), P/Nb-CeNTs (c), Pb/Nb-CeNTs (d); (b): Nb-CeO<sub>2</sub>(N) (a), K/Nb-CeO<sub>2</sub>(N) (b), P/Nb-CeO<sub>2</sub>(N) (c), Pb/Nb-CeO<sub>2</sub>(N) (d).

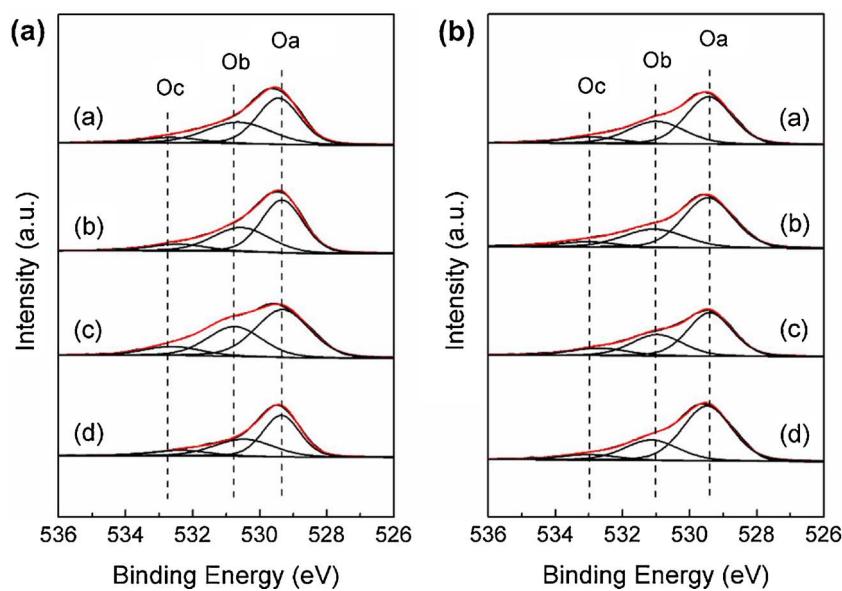


Fig. 7. XPS spectra of O1s (a): Nb-CeNTs (a), K/Nb-CeNTs (b), P/Nb-CeNTs (c), Pb/Nb-CeNTs (d); (b): Nb-CeO<sub>2</sub>(N) (a), K/Nb-CeO<sub>2</sub>(N) (b), P/Nb-CeO<sub>2</sub>(N) (c), Pb/Nb-CeO<sub>2</sub>(N) (d).

**Table 3**  
Valence proportions calculated from fitted XPS spectra.

Catalyst	Nb <sup>4+</sup> /Nb <sup>4+</sup> + Nb <sup>5+</sup> (%)	Ce <sup>3+</sup> /Ce <sup>3+</sup> + Ce <sup>4+</sup> (%)	Ob/Oa + Ob + Oc (%)
Nb-CeNTs	32.6	15.7	37.8
K/Nb-CeNTs	27.9	15.2	31.9
P/Nb-CeNTs	31.2	14.5	34.0
Pb/Nb-CeNTs	31.4	20.5	35.7
Nb-CeO <sub>2</sub> (N)	29.9	15.7	33.4
K/Nb-CeO <sub>2</sub> (N)	25.4	15.4	29.0
P/Nb-CeO <sub>2</sub> (N)	28.7	16.4	31.7
Pb/Nb-CeO <sub>2</sub> (N)	23.0	15.6	27.0

CeO<sub>2</sub>(N) are same. However, they differ after poisons doping. For Nb-CeNTs, the proportion of Ce<sup>3+</sup> in the total cerium both decrease once potassium and phosphorus are added, especially after phosphorus doping. From the XRD, TEM, and BET analysis, the phosphorus slightly affects the structure of ceria nanotubes. This is further verified by the results of XPS Ce 3d that show the addition of phosphorus will influence the chemical valence of cerium. In contrast, the proportion of Ce<sup>3+</sup> species increases for Pb/Nb-CeNTs, which may be another reason why Nb-CeNTs exhibits the best resistance to lead. For Nb-CeO<sub>2</sub>(N) series, the proportions of Ce<sup>3+</sup> both decrease after potassium and lead doping but increase a little for P/Nb-CeO<sub>2</sub>(N). As the Nb-CeO<sub>2</sub>(N) shows excellent resistance against P but inferior resistance to K and Pb, the change in proportion of Ce<sup>3+</sup> is well related to the resistance performance. The SCR activity and resistance ability are not only determined by the Nb species but also the cerium support. The synergistic effect between CeNTs and Nb<sub>2</sub>O<sub>5</sub> as well as the protection of ceria nanotubes contribute to a remarkable NO<sub>x</sub> reduction rate and resistance against K, P, and Pb.

The O 1s XPS spectra in Fig. 7 are also deconvoluted into several separate small peaks. The peak at 529.6 eV (labelled as Oa) is attributed to the lattice oxygen, the one at 530.6 eV is assigned to chemisorbed oxygen (labelled as Ob), and the peak at 531.6 eV (labelled as Oc) is due to structural H<sub>2</sub>O or OH groups [36,46,47]. As mentioned above, chemisorbed oxygen can fill up the oxygen defects and thus accelerate the Nb<sup>5+</sup>/Nb<sup>4+</sup> as well as Ce<sup>4+</sup>/Ce<sup>3+</sup> redox cycles. Therefore, the content of chemisorbed oxygen species is calculated from the individual peak areas in Fig. 7, with the results listed in Table 3. The content of Ob shows a quite similar tendency to that of Nb<sup>4+</sup>. The Nb-CeNTs (37.8%)

has more chemisorbed oxygen than Nb-CeO<sub>2</sub>(N) (33.4%). Once poisons are introduced into Nb-CeNTs, P/Nb-CeNTs and Pb/Nb-CeNTs maintain more Ob than K/Nb-CeNTs. Moreover, the chemisorbed oxygen in K/Nb-CeO<sub>2</sub>(N) and Pb/Nb-CeO<sub>2</sub>(N) also decline, but that in P/Nb-CeO<sub>2</sub>(N) only has a small loss. The variation of Ob in all these catalysts resemble the distribution of Nb<sup>4+</sup> species in Nb<sub>2</sub>O<sub>5</sub>, further revealing that the utilization of ceria nanotubes prevent the poisons attacking the active phase inside the nanotubes.

The H<sub>2</sub>-TPR experiment is conducted to investigate the redox properties and oxygen mobility of all the samples (Fig. 8). The two peaks at 596 °C and 730 °C generating in the reduction curve of CeNTs are ascribed to the reduction of surface oxygen (surface Ce<sup>4+</sup> to Ce<sup>3+</sup>) and bulk oxygen (bulk Ce<sup>4+</sup> to Ce<sup>3+</sup>), respectively [48–50]. For CeO<sub>2</sub>(N), these two peaks shift to 502 °C and 776 °C, respectively, indicating that the surface oxygen is easier to be reduced while the bulk oxygen becomes more stable. Furthermore, the H<sub>2</sub> consumption of CeNTs and CeO<sub>2</sub>(N) are 36.5 and 19.4 μmol/g, respectively, suggesting that CeNTs has stronger redox ability. And the reduced CeO<sub>2</sub> into Ce<sub>2</sub>O<sub>3</sub> have been calculated to be 3.65 and 1.94 μmol for CeNTs and CeO<sub>2</sub>(N), respectively. In addition, it is reported that the reduction peak of Nb<sub>2</sub>O<sub>5</sub> is about 873 °C, which is responsible for the reduction of bulk Nb<sub>2</sub>O<sub>5</sub> to Nb<sub>2</sub>O<sub>4</sub> [27]. Although no obvious reduction peak is detected at this temperature, we can see that the reduction peaks of Nb-CeNTs shift to lower temperatures, revealing that the addition of niobium species makes the reduction reaction easier. For Nb-CeO<sub>2</sub>(N), the reduction peaks shift towards higher temperatures than those of Nb-CeNTs, especially the one at 746 °C. Moreover, the H<sub>2</sub> consumption of Nb-CeNTs and Nb-CeO<sub>2</sub>(N) are 46.9 and 42.1 μmol/g, respectively, revealing that the doping of niobia increases the redox capacity and Nb-CeNTs is a better catalyst. After exposure to different poisons, all the reduction peaks shift to higher temperatures, indicating that the poisons combine with supports or niobium species. To accurately compare the redox properties of all catalysts and study the influence of ceria nanotubes and ceria nanoparticles on the resistance performance, the H<sub>2</sub> consumption of all reduction peaks are calculated for each sample. When K, P, and Pb is introduced individually into the catalyst, the H<sub>2</sub> consumption decreases to 39.9, 44.4, 40.6 μmol/g for K/Nb-CeNTs, P/Nb-CeNTs, Pb/Nb-CeNTs, respectively. It is revealed that the addition of K inflicts more serious damage to the redox properties of Nb-CeNTs than P and Pb. For the Nb-CeO<sub>2</sub>(N) series, the H<sub>2</sub> consumption decline to 39.0, 40.7, 38.6 μmol/g for K/Nb-CeO<sub>2</sub>(N), P/Nb-CeO<sub>2</sub>(N), Pb/Nb-CeO<sub>2</sub>(N), respectively. Among these, K and Pb affect the redox

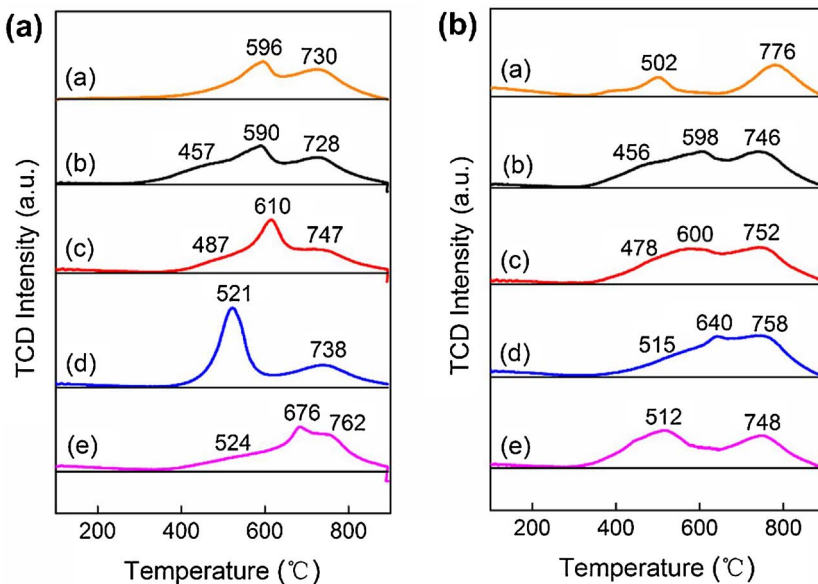


**Fig. 8.** H<sub>2</sub>-TPR plot of (a): CeNTs (a), Nb-CeNTs (b), K/Nb-CeNTs (c), P/Nb-CeNTs (d), Pb/Nb-CeNTs (e); (b): CeO<sub>2</sub>(N) (a), Nb-CeO<sub>2</sub>(N) (b), K/Nb-CeO<sub>2</sub>(N) (c), P/Nb-CeO<sub>2</sub>(N) (d), Pb/Nb-CeO<sub>2</sub>(N) (e).

properties of Nb-CeO<sub>2</sub>(N) much more than P. The redox properties of these catalysts also agree with the results of the SCR performance very well, indicating that the redox capacity of catalysts plays a crucial role for the SCR activity and resistance performance.

#### 3.4. Surface acidity analysis

It is generally accepted that abundant acidic sites is an important factor for the SCR reaction with NH<sub>3</sub>. To investigate the specific surface acid sites and precisely study the role of acidic species in all of these samples, NH<sub>3</sub> DRIFT adsorption spectra (NH<sub>3</sub>-FTIR) are collected at 100 °C (Fig. 9). The bands at 1100–1300 cm<sup>-1</sup>, 1500–1750 cm<sup>-1</sup> are ascribed to NH<sub>3</sub> adsorb on Lewis acidic sites [51–53], while those at 1340–1560 cm<sup>-1</sup> are assigned to NH<sub>4</sub><sup>+</sup> species adsorb on Brønsted acidic sites [52,54–57]. It can be observed that the Lewis acidic sites are the main species for Nb-CeNTs and Nb-CeO<sub>2</sub>(N). Moreover, the Nb-CeO<sub>2</sub>(N) sample has more Lewis acidic sites than Nb-CeNTs. After K, P, and Pb are added into the fresh catalysts, the Lewis acidic sites do not change for K/Nb-CeNTs but the Brønsted acidic sites greatly loss. The Brønsted acidic sites on P/Nb-CeNTs and Pb/Nb-CeNTs almost remain

the same, but the Lewis acidic sites decrease for P/Nb-CeNTs and even vanish for Pb/Nb-CeNTs. Considering the NO<sub>x</sub> reduction activity of these samples, the Brønsted acidic sites are the “valid” acidic sites species for Nb-CeNTs based catalyst. For the poisoned Nb-CeO<sub>2</sub>(N) samples, the ones that have inferior NO<sub>x</sub> conversion also suffer serious damage to Brønsted acidic sites, such as K/Nb-CeO<sub>2</sub>(N) and Pb/Nb-CeO<sub>2</sub>(N). However, P/Nb-CeO<sub>2</sub>(N) still possesses plenty of Brønsted acidic sites and even more than those on Nb-CeO<sub>2</sub>(N). In spite of the lack of Lewis acidic sites for P/Nb-CeO<sub>2</sub>(N), it still yields the best SCR activity among the poisoned Nb-CeO<sub>2</sub>(N) catalysts, indicating that Brønsted acidic sites are also important in this series. Finally, the Nb-CeNTs has more Brønsted acidic sites than Nb-CeO<sub>2</sub>(N), and the poisons show little effect on the acidic sites of Nb-CeNTs. Thus, the Nb-CeNTs catalyst achieves excellent resistance and demonstrates the advantage of ceria nanotubes in the SCR reaction.

In summary, the nanotubular structure of the ceria nanotubes can provide a “shell” to prevent the active phase, niobia, as the “core” from being poisoned by different poisons (K, P, and Pb). Otherwise, if the support material is replaced by ceria nanoparticles, the poisons will interact with the active phase and carrier quite easily. Thus, the

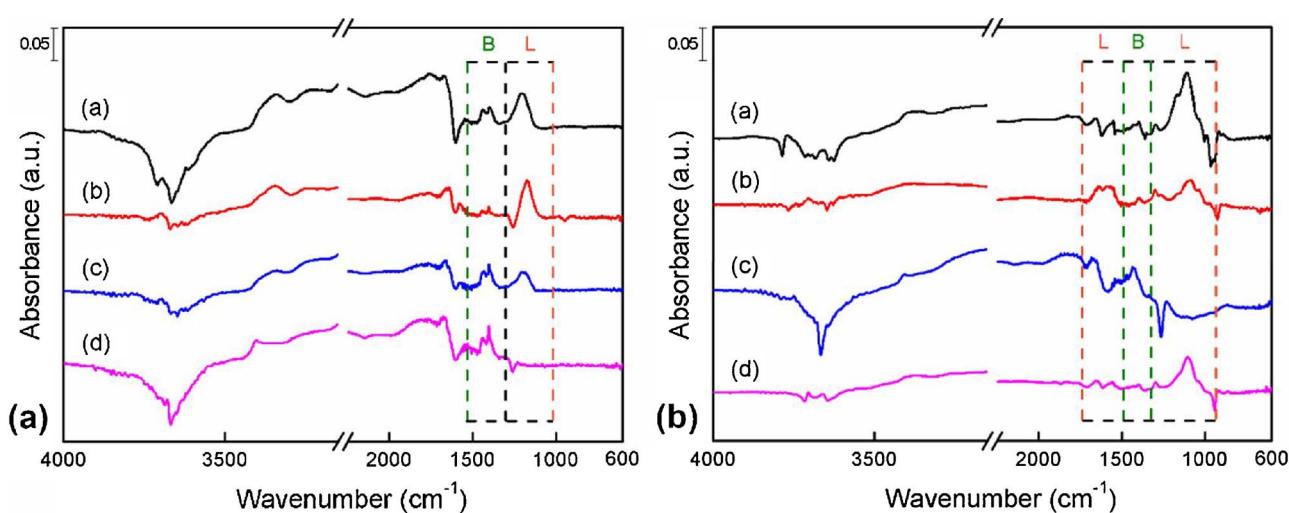
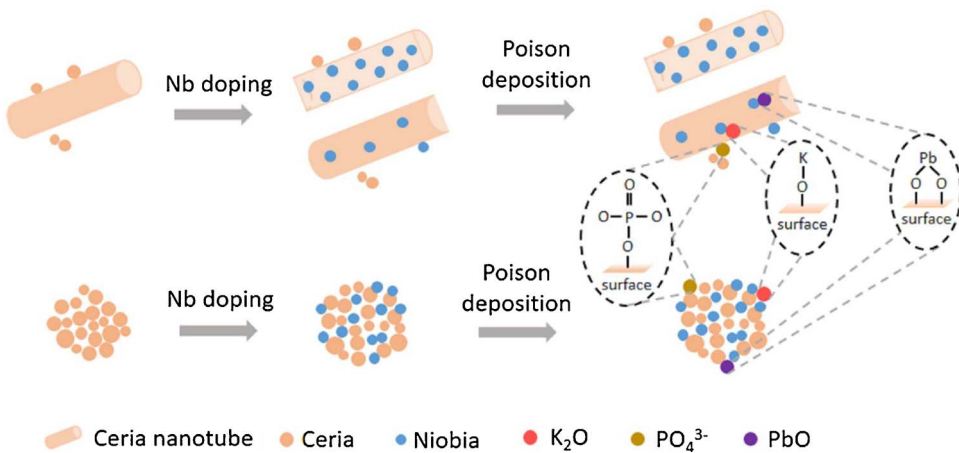


**Fig. 9.** NH<sub>3</sub>-FTIR plot of (a): Nb-CeNTs (a), K/Nb-CeNTs (b), P/Nb-CeNTs (c), Pb/Nb-CeNTs (d); (b): Nb-CeO<sub>2</sub>(N) (a), K/Nb-CeO<sub>2</sub>(N) (b), P/Nb-CeO<sub>2</sub>(N) (c), Pb/Nb-CeO<sub>2</sub>(N) (d).



Scheme 2. Promotional mechanism of the enhanced resistance (K, P, Pb) of Nb-CeNTs.

presence of nanotubes affect the physical and chemical properties of deNO<sub>x</sub> catalyst and increase their resistance to poisons of K, P, and Pb. Based on the deactivation model of V<sub>2</sub>O<sub>5</sub>-WO<sub>3</sub>/TiO<sub>2</sub> monolith catalyst that Olsen, B. K. et al. proposed and the results we obtained above [58–60], the promotional mechanism of enhanced resistance (K, P, Pb) of Nb-CeNTs and poisoning mechanism of Nb-CeO<sub>2</sub>(N) are both shown in Scheme 2.

#### 4. Conclusions

In this work, we demonstrate that the combination of niobia and ceria nanotubes shows better synergistic effect than niobia doping on ceria nanoparticles, with a higher SCR activity and remarkable resistance to three different kinds of poisons: potassium, phosphorus, and lead. Experimental results show that NO<sub>x</sub> conversion of Nb-CeNTs exceeds 90% in a broad temperature region of 275–450 °C while Nb-CeO<sub>2</sub>(N) only obtains the highest reduction rate of 90% at 350 °C and then declines once temperature increases. After the introduction of K, P, and Pb, the K/Nb-CeNTs, P/Nb-CeNTs, Pb/Nb-CeNTs still reveal excellent performance (at 78%, 90% and 97%, respectively) in NO<sub>x</sub> conversion. However, the NO<sub>x</sub> conversion of poisoned Nb-CeO<sub>2</sub>(N) catalysts express sharp decline except P/Nb-CeO<sub>2</sub>(N). K/Nb-CeO<sub>2</sub>(N) and Pb/Nb-CeO<sub>2</sub>(N) merely yield NO<sub>x</sub> removal rates of 35% and 20%, respectively. From the characterization results of XRD, TEM, BET, XPS, H<sub>2</sub>-TPR, and NH<sub>3</sub>-FTIR, it is concluded that the ceria nanotubes with nanotubular structure absolutely predominate the resistance performance of SCR catalyst as the CeNTs and CeO<sub>2</sub>(N) possess similar crystal phases and surface area. Therefore, the well-maintained structure of CeNTs plays a crucial role in the reduction reaction. Furthermore, the doped niobia not only improve the redox ability and acidic sites of CeNTs but also help to maintain the smooth Nb<sup>5+</sup>/Nb<sup>4+</sup> and Ce<sup>4+</sup>/Ce<sup>3+</sup> redox cycles, superior redox capacity, and abundant surface Brønsted acidic sites after introduction of poisons into Nb-CeNTs. Thus, the ceria nanotubes confining niobia catalyst achieve overwhelming SCR activity and resistance to K, P, and Pb. We expect that the work conducts herein can contribute to making the SCR process more reliable in applications involving high amounts of alkali metals, phosphorus compounds, and heavy metals, e.g. the flue gases in refuse incinerator, cement plants, glass furnaces, and biomass power plants.

#### Acknowledgements

This research was financially supported by National Key Research and Development Plan (2016YFC0204101), National Natural Science Foundation of China (NSFC-51278458), Key Project of Zhejiang Provincial Science and Technology Program, Zhejiang Provincial “151” Talents Program, the Program for Zhejiang Leading Team of S&T

Innovation (Grant No. 2013TD07) and Changjiang Scholar Incentive Program (Ministry of Education, China, 2009).

#### Appendix A. Supplementary data

Supplementary material related to this article can be found, in the online version, at doi:<https://doi.org/10.1016/j.apcatb.2018.03.024>.

#### References

- [1] M. Klimczak, P. Kern, T. Heinzelmann, M. Lucas, P. Claus, High-throughput study of the effects of inorganic additives and poisons on NH<sub>3</sub>-SCR catalysts part I: V<sub>2</sub>O<sub>5</sub>-WO<sub>3</sub>/TiO<sub>2</sub> catalysts, *Appl. Catal. B-Environ.* 95 (2010) 39–47.
- [2] P. Kern, M. Klimczak, T. Heinzelmann, M. Lucas, P. Claus, High-throughput study of the effects of inorganic additives and poisons on NH<sub>3</sub>-SCR catalysts. Part II: Fe zeolite catalysts, *Appl. Catal. B-Environ.* 95 (2010) 48–56.
- [3] G. Carja, G. Delahay, C. Signorile, B. Coq, Fe-Ce-ZSM-5 a new catalyst of outstanding properties in the selective catalytic reduction of NO with NH<sub>3</sub>, *Chem. Commun.* (2004) 1404–1405.
- [4] R.Q. Long, R.T. Yang, Superior Fe-ZSM-5 catalyst for selective catalytic reduction of nitric oxide by ammonia, *J. Am. Chem. Soc.* 121 (1999) 5595–5596.
- [5] Z. Huang, X. Gu, W. Wen, P. Hu, M. Makkee, H. Lin, F. Kapteijn, X. Tang, A “smart” hollandite DeNO<sub>x</sub> catalyst: self-protection against alkali poisoning, *Angew. Chem. Int. Edit.* 52 (2013) 660–664.
- [6] Y. Peng, J. Li, L. Chen, J. Chen, J. Han, H. Zhang, W. Han, Alkali metal poisoning of a CeO<sub>2</sub>-WO<sub>3</sub> catalyst used in the selective catalytic reduction of NO<sub>x</sub> with NH<sub>3</sub>: an experimental and theoretical study, *Environ. Sci. Technol.* 46 (2012) 2864–2869.
- [7] F. Tang, B. Xu, H. Shi, J. Qiu, Y. Fan, The poisoning effect of Na<sup>+</sup> and Ca<sup>2+</sup> ions doped on the V<sub>2</sub>O<sub>5</sub>/TiO<sub>2</sub> catalysts for selective catalytic reduction of NO by NH<sub>3</sub>, *Appl. Catal. B-Environ.* 94 (2010) 71–76.
- [8] H. Chang, M.T. Jong, C. Wang, R. Qu, Y. Du, J. Li, J. Hao, Design strategies for P-containing fuels adaptable CeO<sub>2</sub>-MoO<sub>3</sub> catalysts for DeNO<sub>x</sub>: significance of phosphorus resistance and N<sub>2</sub> selectivity, *Environ. Sci. Technol.* 47 (2013) 11692–11699.
- [9] K. Sun, Q. Zhong, A. Yu, The study of the deactivation of SCR catalysts, *Chin. Environ. Prot. Ind.* (2008) 40–42.
- [10] R. Guo, C. Lu, W. Pan, W. Zhen, Q. Wang, Q. Chen, H. Ding, N. Yang, A comparative study of the poisoning effect of Zn and Pb on Ce/TiO<sub>2</sub> catalyst for low temperature selective catalytic reduction of NO with NH<sub>3</sub>, *Catal. Commun.* 59 (2015) 136–139.
- [11] R. Khodayari, C.I. Odenbrand, Deactivating effects of lead on the selective catalytic reduction of nitric oxide with ammonia over a V<sub>2</sub>O<sub>5</sub>/WO<sub>3</sub>/TiO<sub>2</sub> catalyst for waste incineration applications, *Ind. Eng. Chem. Res.* 37 (1998) 1196–1202.
- [12] Y. Jiang, X. Gao, Y. Zhang, W. Wu, H. Song, Z. Luo, K. Cen, Effects of PbCl<sub>2</sub> on selective catalytic reduction of NO with NH<sub>3</sub> over vanadia-based catalysts, *J. Hazard. Mater.* 274 (2014) 270–278.
- [13] D. Chen, S. Zhao, Z. Qu, N. Yan, Cu-BTC as a novel material for elemental mercury removal from sintering gas, *Fuel* 217 (2018) 297–305.
- [14] Z. Qu, L. Fang, D. Chen, H. Xu, N. Yan, Effective and regenerable Ag/graphene adsorbent for Hg(II) removal from aqueous solution, *Fuel* 203 (2017) 128–134.
- [15] B.L. Turner, A.B. Leytem, Phosphorus compounds in sequential extracts of animal manures: chemical speciation and a novel fractionation procedure, *Environ. Sci. Technol.* 38 (2004) 6101–6108.
- [16] J. Zhuo, S. Li, L. Duan, Q. Yao, Effect of phosphorus transformation on the reduction of particulate matter formation during co-combustion of coal and sewage sludge, *Energ. Fuel.* 26 (2012) 3162–3166.
- [17] Y. Zheng, A.D. Jensen, J.E. Johnson, Deactivation of V<sub>2</sub>O<sub>5</sub>-WO<sub>3</sub>-TiO<sub>2</sub> SCR catalyst at a biomass-fired combined heat and power plant, *Appl. Catal. B-Environ.* 60 (2005) 253–264.

[18] S. Kristensen, A. Kunov-Kruse, A. Riisager, S. Rasmussen, R. Fehrmann, High performance vanadia-anatase nanoparticle catalysts for the selective catalytic reduction of NO by ammonia, *J. Catal.* 284 (2011) 60–67.

[19] A. Kling, C. Andersson, A. Myringer, D. Eskilsson, S.G. Jaras, Alkali deactivation of high-dust SCR catalysts used for NO<sub>x</sub> reduction exposed to flue gas from 100 MW-scale biofuel and peat fired boilers: influence of flue gas composition, *Appl. Catal. B-Environ.* 69 (2007) 240–251.

[20] D. Nicosia, I. Czekaj, O. Krocher, Chemical deactivation of V<sub>2</sub>O<sub>5</sub>/WO<sub>3</sub>-TiO<sub>2</sub> SCR catalysts by additives and impurities from fuels lubrication oils and urea solution - part II. characterization study of the effect of alkali and alkaline earth metals, *Appl. Catal. B-Environ.* 77 (2008) 228–236.

[21] J. Beck, J. Brandenstein, S. Unterberger, K.R. Hein, Effects of sewage sludge and meat and bone meal co-combustion on SCR catalysts, *Appl. Catal. B-Environ.* 49 (2004) 15–25.

[22] L. Chen, J. Li, M. Ge, DRIFT study on cerium-tungsten/titania catalyst for selective catalytic reduction of NO<sub>x</sub> with NH<sub>3</sub>, *Environ. Sci. Technol.* 44 (2010) 9590–9596.

[23] S. Gao, X. Chen, H. Wang, J. Mo, Z. Wu, Y. Liu, X. Weng, Ceria supported on sulfated zirconia as a superacid catalyst for selective catalytic reduction of NO with NH<sub>3</sub>, *J. Colloid Interf. Sci.* 394 (2013) 515–521.

[24] D. Zhang, L. Zhang, L. Shi, C. Fang, H. Li, R. Gao, L. Huang, J. Zhang, In situ supported MnO<sub>x</sub>-CeO<sub>x</sub> on carbon nanotubes for the low-temperature selective catalytic reduction of NO with NH<sub>3</sub>, *Nanoscale* 5 (2013) 1127–1136.

[25] X. Chen, H. Wang, Z. Wu, Y. Liu, X. Weng, Novel H<sub>2</sub>Ti<sub>12</sub>O<sub>25</sub>-confined CeO<sub>2</sub> catalyst with remarkable resistance to alkali poisoning based on the “shell protection effect”, *J. Phys. Chem. C* 115 (2011) 17479–17484.

[26] Z. Ma, X. Wu, Z. Si, D. Weng, J. Ma, T. Xu, Impacts of niobia loading on active sites and surface acidity in NbO<sub>x</sub>/CeO<sub>2</sub>-ZrO<sub>2</sub> NH<sub>3</sub>-SCR catalysts, *Appl. Catal. B-Environ.* 179 (2015) 380–394.

[27] S. Ding, F. Liu, X. Shi, H. He, Promotional effect of Nb additive on the activity and hydrothermal stability for the selective catalytic reduction of NO<sub>x</sub> with NH<sub>3</sub> over CeZrO<sub>x</sub> catalyst, *Appl. Catal. B-Environ.* 180 (2016) 766–774.

[28] X. Du, X. Gao, Y. Fu, F. Gao, Z. Luo, K. Cen, The co-effect of Sb and Nb on the SCR performance of the V<sub>2</sub>O<sub>5</sub>/TiO<sub>2</sub> catalyst, *J. Colloid Interf. Sci.* 368 (2012) 406–412.

[29] R. Qu, Y. Peng, X. Sun, J. Li, X. Gao, K. Cen, Identification of the reaction pathway and reactive species for the selective catalytic reduction of NO with NH<sub>3</sub> over cerium-niobium oxide catalysts, *Catal. Sci. Technol.* 6 (2016) 2136–2142.

[30] P. Wang, H. Wang, X. Chen, Z. Wu, Design strategies for a denitrification catalyst with improved resistance against alkali poisoning: the significance of nanoconfining spaces and acid-base balance, *ChemCatChem* 8 (2016) 787–797.

[31] P. Wang, H. Wang, X. Chen, Y. Liu, X. Weng, Z. Wu, Novel SCR catalyst with superior alkaline resistance performance: enhanced self-protection originated from modifying protonated titanate nanotubes, *J. Mater. Chem. A* 3 (2015) 680–690.

[32] H. Wang, P. Wang, X. Chen, Z. Wu, Uniformly active phase loaded selective catalytic reduction catalysts (V<sub>2</sub>O<sub>5</sub>/TNTs) with superior alkaline resistance performance, *J. Hazard. Mater.* 324 (2016) 507–515.

[33] X. Zhao, J. You, X. Lu, Z. Chen, Hydrothermal synthesis, characterization and property of CeO<sub>2</sub> nanotube, *J. Inorg. Mater.* 26 (2011) 159–164.

[34] X. Liu, W. Wei, Q. Yuan, X. Zhang, N. Li, Y. Du, G. Ma, C. Yan, D. Ma, Apoferritin-CeO<sub>2</sub> nano-truffle that has excellent artificial redox enzyme activity, *Chem. Commun.* 48 (2012) 3155–3157.

[35] S. Gao, P. Wang, X. Chen, H. Wang, Z. Wu, Y. Liu, X. Weng, Enhanced alkali resistance of CeO<sub>2</sub>/SO<sub>4</sub><sup>2-</sup>-ZrO<sub>2</sub> catalyst in selective catalytic reduction of NO<sub>x</sub> by ammonia, *Catal. Commun.* 43 (2013) 223–226.

[36] H. Wang, X. Chen, S. Gao, Z. Wu, Y. Liu, X. Weng, Deactivation mechanism of Ce/TiO<sub>2</sub> selective catalytic reduction catalysts by the loading of sodium and calcium salts, *Catal. Sci. Technol.* 3 (2013) 715–722.

[37] L. Chen, J. Li, W. Ablikim, J. Wang, H. Chang, L. Ma, J. Xu, M. Ge, H. Arandiyan, CeO<sub>2</sub>-WO<sub>3</sub> mixed oxides for the selective catalytic reduction of NO<sub>x</sub> by NH<sub>3</sub> over a wide temperature range, *Catal. Lett.* 141 (2011) 1859–1864.

[38] L. Ma, J. Li, H. Arandiyan, W. Shi, C. Liu, L. Fu, Influence of calcination temperature on Fe/HBEA catalyst for the selective catalytic reduction of NO<sub>x</sub> with NH<sub>3</sub>, *Catal. Today* 184 (2012) 145–152.

[39] C.O. Olsson, D. Landolt, Atmospheric oxidation of a Nb-Zr alloy studied with XPS, *Corros. Sci.* 46 (2004) 213–224.

[40] E. Beche, P. Charvin, D. Perarnau, S. Abanades, G. Flamant, Ce 3d XPS investigation of cerium oxides and mixed cerium oxide (Ce<sub>x</sub>Ti<sub>y</sub>O<sub>z</sub>), *Surf. Interface Anal.* 40 (2008) 264–267.

[41] F. Larachi, J. Pierre, A. Adnot, A. Bernis, Ce 3d XPS study of composite Ce<sub>x</sub>Mn<sub>1-x</sub>O<sub>2-y</sub> wet oxidation catalysts, *Appl. Surf. Sci.* 195 (2002) 236–250.

[42] C.T. Campbell, C.H.F. Peden, Oxygen vacancies and catalysis on ceria surfaces, *Science* 309 (2005) 713–714.

[43] F. Esch, S. Fabris, L. Zhou, T. Montini, C. Africh, P. Fornasiero, G. Comelli, R. Rosei, Electron localization determines defect formation on ceria substrates, *Science* 309 (2005) 752–755.

[44] P. Dutta, S. Pal, M.S. Seehra, Y. Shi, E.M. Eyring, R.D. Ernst, Concentration of Ce<sup>3+</sup> and oxygen vacancies in cerium oxide nanoparticles, *Chem. Mater.* 18 (2006) 5144–5146.

[45] X. Liu, K. Zhou, L. Wang, B. Wang, Y. Li, Oxygen vacancy clusters promoting reducibility and activity of ceria nanorods, *J. Am. Chem. Soc.* 131 (2009) 3140–3141.

[46] H. Wang, S. Cao, C. Cen, X. Chen, Z. Wu, Structure-activity relationship of titanate nanotube-confined ceria catalysts in selective catalytic reduction of NO with ammonia, *Catal. Lett.* 143 (2013) 1312–1318.

[47] X. Chen, H. Wang, S. Gao, Z. Wu, Effect of pH value on the microstructure and deNO<sub>x</sub> catalytic performance of titanate nanotubes loaded CeO<sub>2</sub>, *J. Colloid Interf. Sci.* 377 (2012) 131–136.

[48] B. Murugan, A.V. Ramaswamy, Chemical states and redox properties of Mn/CeO<sub>2</sub>-TiO<sub>2</sub> nanocomposites prepared by solution combustion route, *J. Phys. Chem. C* 112 (2008) 20429–20442.

[49] S. Yang, Y. Guo, H. Chang, L. Ma, Y. Peng, Z. Qu, N. Yan, C. Wang, J. Li, Novel effect of SO<sub>2</sub> on the SCR reaction over CeO<sub>2</sub>: mechanism and significance, *Appl. Catal. B-Environ.* 136 (2013) 19–28.

[50] F. Wyrwalski, J.M. Giraudon, J.F. Lamonier, Synergistic coupling of the redox properties of supports and cobalt oxide Co<sub>3</sub>O<sub>4</sub> for the complete oxidation of volatile organic compounds, *Catal. Lett.* 137 (2010) 141–149.

[51] B. Jiang, Z. Wu, Y. Liu, S. Lee, W. Ho, DRIFT study of the SO<sub>2</sub> effect on low-temperature SCR reaction over Fe-Mn/TiO<sub>2</sub>, *J. Phys. Chem. C* 114 (2010) 4961–4965.

[52] Y. Liu, T. Gu, X. Weng, Y. Wang, Z. Wu, H. Wang, DRIFT studies on the selectivity promotion mechanism of Ca-modified Ce-Mn/TiO<sub>2</sub> catalysts for low-temperature NO reduction with NH<sub>3</sub>, *J. Phys. Chem. C* 116 (2012) 16582–16592.

[53] S. Ding, F. Liu, X. Shi, K. Liu, L. Xie, H. He, Significant promotion effect of Mo additive on a novel Ce-Zr mixed oxide catalyst for the selective catalytic reduction of NO<sub>x</sub> with NH<sub>3</sub>, *ACS Appl. Mater. Interf.* 7 (2015) 9497–9506.

[54] W.S. Kijlstra, D.S. Brands, E.K. Poels, A. Blieck, Mechanism of the selective catalytic reduction of NO by NH<sub>3</sub> over MnO<sub>x</sub>/Al<sub>2</sub>O<sub>3</sub>, *J. Catal.* 171 (1997) 208–218.

[55] X. Wang, A. Shi, Y. Duan, J. Wang, M. Shen, Catalytic performance and hydrothermal durability of CeO<sub>2</sub>-V<sub>2</sub>O<sub>5</sub>-ZrO<sub>2</sub>/WO<sub>3</sub>-TiO<sub>2</sub> based NH<sub>3</sub>-SCR catalysts, *Catal. Sci. Technol.* 2 (2012) 1386–1395.

[56] L. Chen, J. Li, M. Ge, The poisoning effect of alkali metals doping over nano V<sub>2</sub>O<sub>5</sub>-WO<sub>3</sub>/TiO<sub>2</sub> catalysts on selective catalytic reduction of NO<sub>x</sub> by NH<sub>3</sub>, *Chem. Eng. J.* 170 (2011) 531.

[57] L. Chen, J. Li, M. Ge, L. Ma, H. Chang, Mechanism of selective catalytic reduction of NO<sub>x</sub> with NH<sub>3</sub> over CeO<sub>2</sub>-WO<sub>3</sub> catalysts, *Chin. J. Catal.* 32 (2011) 836–841.

[58] B.K. Olsen, F. Kügler, F. Castellino, L. Schill, A.D. Jensen, Deactivation of SCR Catalysts by Potassium: A Study of Potential Alkali Barrier Materials, Vgb Powertech, 2017, pp. 56–64.

[59] B.K. Olsen, F. Castellino, A.D. Jensen, Modeling deactivation of catalysts for selective catalytic reduction of NO<sub>x</sub> by KCl aerosols, *Ind. Eng. Chem. Res.* 56 (2017) 13020–13033.

[60] B.K. Olsen, F. Kügler, F. Castellino, A.D. Jensen, Poisoning of vanadia based SCR catalysts by potassium: influence of catalyst composition and potassium mobility, *Catal. Sci. Technol.* 6 (2016) 2249–2260.